



Zeolite-supported nickel phyllosilicate catalyst for C–O hydrogenolysis of cyclic ethers and polyols

Elmira Soghrati^{a,b}, Theodore Kay Chen Ong^a, Chee Kok Poh^a, Sibudjing Kawi^{b,*}, Armando Borgna^{a,*}

^a Heterogeneous Catalysis Division, Institute of Chemical and Engineering Sciences, Agency for Science, Technology, and Research, 1 Pesek Road, Jurong Island, 627833, Singapore

^b Department of Chemical and Biomolecular Engineering, National University of Singapore, 4 Engineering Drive 4, 117585, Singapore

ARTICLE INFO

Keywords:

Hydrogenolysis
Nickel
Phyllosilicate
Zeolite
Confinement effect

ABSTRACT

In this study, a series of zeolites, including small pore (SAPO-34), medium pore (Ferrierite, ZSM-5, and ZSM-11), and large pore (MOR and BETA) zeolites were explored as supports for nickel catalysts. The catalysts were prepared by the deposition–precipitation (D–P) method to obtain ca. 10 wt% Ni loading. The structures of prepared catalysts were elucidated using a wide range of characterization techniques such as BET, XRD, TEM, H₂-TPR, NH₃-TPD, FTIR, and XPS. It was found that 1:1 nickel phyllosilicate structures is formed over D–P nickel catalysts, while 2:1 nickel phyllosilicate was identified only over Ni/BETA catalyst. Furthermore, Ni/ZSM-5 catalyst was also prepared by impregnation method as a reference to investigate the effect of preparation method. The impact of the topological structures of zeolite on the catalytic activity of reactants (i.e., cyclic ethers derived from furanic compounds), reaction intermediates (i.e., polyols) was subsequently investigated. The ring-opening of THFA can proceed over Ni/Ni phyllosilicate species on the external surface of the catalyst, producing pentane polyols. Then, the pentane polyol intermediates can further undergo ring-closure pathway, predominantly over the internal acid sites within zeolite structures (except for Ni/SAPO-34). It was found that medium-pore zeolites (ZSM-5 and ZSM-11) with mild acidity exhibit the highest reaction rate with a THP yield up to ca. 64%. Similarly, the highest catalytic activity during THPM conversion was achieved over ZSM-5- and ZSM-11-supported nickel catalysts, with up to 51% selectivity towards 16HDO. Comparing the zeolite maximum pore sizes and the kinetic diameters of the reactants and products with the catalytic performance, it is clear that topological structures of ZSM-5 and ZSM-11 have pore confinement effect on the reaction mechanism and catalytic activity in the hydrogenolysis of cyclic ethers and polyols.

1. Introduction

The dependence of the chemical industry on traditional oil feedstocks is of growing concern, especially when oil reserves are continually being depleted. Furthermore, the environmental hazards that the usage of oil poses have become a strong motivation for the development of environmentally friendlier, bio-renewable feedstock for the chemical industry [1]. Furanic compounds and their derivatives have been well established as a bio-renewable feedstock for the production of a wide range of high value-added chemicals [2]. As a well-known example, furfural can be obtained from acid-catalyzed dehydration of pentoses obtained from plant biomass [3,4]. Tetrahydrofurfuryl alcohol (THFA), which can be produced from the total hydrogenation of furfural over Ni-based catalysts [5,6], can then undergo ring opening to form 1,5-Pentanediol (15PDO) when the ring-opening is catalyzed by

noble metals such as Rh or Ir modified by Mo or Re oxide [7–10]. Similarly, 5-hydroxymethyl furfural (HMF) can undergo sequential hydrogenation and ring-opening to produce value-added 1,6-hexanediol (16HDO) [11]. These linear carbon chains with both terminal OH groups, known as α,ω -diols, are widely used as monomers for the production of polyesters and polyurethanes.

For such ring-opening reactions, catalysis by noble metals have been extensively studied. However, due to the rarity and price of such metals, it is desired to use non-noble metals as potential replacements for these catalysts. A pioneer work developed a multiple approach to synthesize 15PDO from THFA via a dehydration–hydration–hydrogenation pathway, with an overall yield of ca. 70% [12]. Very recently, this process has been modified by Dumesic et al. for the production of 15PDO from biomass-derived THFA over inexpensive catalysts, reaching a significantly higher overall yield of 90% [13]. The

* Corresponding authors.

E-mail addresses: chekawis@nus.edu.sg (S. Kawi), armando_borgna@ices.a-star.edu.sg (A. Borgna).

process consists of the following three steps: (1) dehydration of THFA to 3,4-2H-dihydropyran (DHP) over γ -Al₂O₃ in the vapor phase; (2) hydration of DHP to 2-hydroxytetrahydropyran (2-HTHP) without addition of any external catalyst in the liquid phase; and (3) ring-opening tautomerization of 2-HTHP to δ -hydroxyvaleraldehyde which can be subsequently hydrogenated into 15PDO over Ru catalysts. Similar multi-step approach was applied to ring-opening of tetrahydropyran-2-methanol (THPM) into 16HDO, resulting in a maximum 34% overall yield of 16HDO [14].

Our previous study [15] has demonstrated that Ni itself is capable of ring opening of THFA at the more sterically hindered secondary C–O bond, yielding mostly 15 PDO along with 1,2,5-pentanetriol (125PTO), which was identified for the first time in aqueous-phase hydrogenolysis of THFA at high temperatures. Furthermore, nickel supported on ZSM-5 is a promising candidate as an inexpensive catalyst with high chemoselectivity for both ring-opening and ring-closure, yielding tetrahydropyran (THP). THP has a wide range of applications as a solvent or as an intermediate in organic synthesis to produce glutaric acid, 1,5-dichloropentane, heptanediamine, and pimelic acid [16,17]. Additionally, it can undergo ring-opening/dehydration to produce pentadienes [18]. The key advantage of this route is the use of a relatively cheap non-noble metal such as Ni in the direct synthesis of THP from THFA. Therefore, it is important to further explore the factors affecting the performance of such Ni-based catalysts.

One of the most critical factors affecting catalyst activity is the catalyst preparation method [19,20]. Nickel–zeolite catalysts are typically prepared by the relatively simple incipient wetness impregnation (IWI) method. However, catalysts prepared by impregnation methods typically suffer from relatively low metal dispersion and hence low catalytic activity [21]. To improve the dispersion and activity of the nickel–zeolite catalysts, the ion exchange and deposition–precipitation (D–P) method [22–25] were studied and it was found that those methods are able to boost higher initial activity and recyclability after repeated runs as compared to impregnation, particularly when using organic solvents [23]. One key reason for this difference is the improved degree of dispersion of nickel on the support surface for the latter two methods as compared to the impregnation one. However, ion exchange method is limited to relatively low metal loading. Previous studies also reported the presence of different nickel species, including nickel hydroxide, nickel oxide, nickel phyllosilicate species, in zeolite-supported catalyst prepared by D–P method [21–23,26]. Besides, our previous studies showed that the nickel catalysts prepared via phyllosilicate precursor could suppress sintering of nickel particles [27]. Hence, it is of great interest to unravel if this stabilizing effect of highly dispersed nickel using the D–P method leads to a good catalytic performance during ring-opening reactions in liquid (aqueous) phase.

Besides preparation methods, another important factor in catalyst activity and effectiveness is the accessibility to the active sites and the ability of reactants/products to diffuse in/out the pores to reach the active sites. Since the structure of the support directly affects the diffusivity of reactants and products in and out of the pores, the structure of the zeolite may also affect the yield and selectivity of the reaction. The structure also affects the shape selectivity of the catalyst [28], which means that the structure may improve selectivity towards given products. Indeed, the effect of the zeolite structure has already been reported in previous studies using bare zeolites [29] and zeolite-supported Ni catalysts [30,31].

In order to get a better understanding of the physicochemical properties of zeolites on ring-opening reactions, this paper aims to understand the effect of catalyst preparation method (D–P) and zeolite structure of zeolite-supported Ni catalysts on performance and recyclability. To achieve this, various zeolites, including small pore zeolites (SAPO-34), medium pore zeolites (Ferrierite, ZSM-5, and ZSM-11), and large pore zeolites (Mordenite and BETA) were investigated for the hydrogenolysis of cyclic ethers and polyols derived from furanic compounds.

2. Experimental

2.1. Catalyst preparation

The ammonium form of Ferrierite (FER), ZSM-5, Mordenite (MOR) and BETA zeolites with SiO₂/Al₂O₃ ratios of 20, 30, 20, and 25, respectively, were obtained from Zeolyst and used as catalyst support. Nickel (II) Nitrate hexahydrate (98%, Alfa Aesar), Urea (ACS, 99.0–100.5% from Alfa Aesar) were used for catalyst preparation. THFA (99 wt%, Sigma Aldrich), THPM (98%, TCI), 1,2,5-pentanetriol (97%, TCI), 1,5-pentanediol (97%, Sigma Aldrich), 1,2,6-hexanetriol (96 wt%, Sigma Aldrich), and 1,6-hexanediol (99 wt%, Sigma Aldrich) were used as reactants without further purification.

ZSM-11 with a SiO₂/Al₂O₃ ratio of 30 was hydrothermally synthesized using a modified method previously described [32], using tetrabutylammonium bromide (TBABr) as the templating agent. A precursor gel containing NaOH, NaAlO₂, TBABr and colloidal silica (LUDOX HS-40) with a molar oxide composition of 2.9Na₂O:1Al₂O₃:9TBABr:30SiO₂:1260H₂O was prepared. The gel was then transferred into a Teflon-lined autoclave under stirring condition (90 rpm) at 150 °C for three days. The resulting crystalline material was filtered, washed and dried at 70 °C overnight, followed by a calcination step at 540 °C for 6 h. To obtain the NH₄-form zeolite, the calcined sample was exchanged with 1 M NH₄NO₃ solution under reflux condition for 2 h.

SAPO-34 zeolite was prepared as reported in literature with some modifications [33]. Fumed silica, pseudo boehmite and phosphoric acid as silicon, aluminium, and phosphorus sources, respectively and morpholine as structural directing agent were used. The molar composition of final gel was 1.00SiO₂: 0.93Al₂O₃: 0.98 P₂O₅: 1.93 morpholine: 61 H₂O. Pseudo boehmite powder was added slowly into diluted phosphoric acid solution and stirred for 3 h to form composition A. Fumed silica was combined with deionized water and morpholine under stirring to make a clear solution (composition B). The composition B was slowly added to composition A under stirring for 2 h, followed by aging under static condition for 24 h. The resulting gel was transferred into a Teflon-lined autoclave for hydrothermal crystallization at 200 °C for 24 h. After hydrothermal step, the solid product was filtered, washed with deionized water, and dried in air at 70 °C overnight. Finally, the organic template was eliminated by calcination at 550 °C for 6 h. Structural properties of zeolites, including the framework type, porous topology, and pore sizes are summarized in Table S1 (Supplementary Material).

The ammonium form of all zeolites were calcined in air at 500 °C for 4 h to convert them into H-zeolites prior to the deposition–precipitation process. Using a method similar to that reported by Nares et al. [21], 250 mL of a 0.14 M nickel nitrate solution was prepared. 2 g of calcined zeolites was dispersed in 210 mL of the nickel nitrate solution at room temperature to form a suspension (pH ~2). The suspension was then heated under reflux to 70 °C. Concurrently, the remaining 40 mL of the nickel nitrate solution (0.14 M) was used to dissolve the required amount of urea to obtain a 0.42 M solution. At 70 °C, the 40 mL urea nickel nitrate solution was added dropwise into the 210 mL suspension. The solution was further heated to 90 °C, where the decomposition of urea begins, releasing hydroxide anions to start the D–P process. The 250 mL suspensions were then kept at around 90–95 °C for 1 h and then quenched using an ice bath to allow the solution to cool down to ~20 °C. After that, the suspension underwent vacuum filtration and washed with warm DI water (50–60 °C). Besides, to investigate the effect of the urea hydrolysis on the structure of zeolite, the procedure was repeated for ZSM-5 using DI water instead of nickel nitrate solution. ZSM-5 supported nickel catalyst was also prepared by IWI method with a fixed Ni loading (10 wt%) and denoted as Ni/ZSM-5-IWI. The resulting catalysts were then dried at 110 °C overnight, followed by a calcination step at 400 °C for 4 h with a heating rate of 1 °C/min. Before catalytic experiments, the catalysts were reduced at 460 °C for 4 h with a heating rate of 2 °C/min and passivated in 1% O₂ in N₂ at room

temperature.

2.2. Catalyst characterization

The Brunauer–Emmett–Teller (BET) surface areas of the zeolitic supports and Ni catalysts were determined using a Micromeritics ASAP–2020 adsorption apparatus. Samples were degassed overnight in vacuum at 200 °C before nitrogen adsorption at –196 °C.

X-ray Fluorescence (XRF) analysis using a S4 Explorer spectrometer (Bruker AXS) was used to determine the nickel loading.

Powder X-ray diffraction (XRD) analysis was carried out on a Bruker D8 Advance diffractometer using filtered Cu K α radiation ($\lambda = 1.5406 \text{ \AA}$) produced by an X-ray source operating at 35 kV and 40 mA. XRD patterns were recorded in a Bragg angle (2θ) range from 20° to 80°.

The metal particle sizes of the zeolite-supported Ni catalysts were estimated by transmission electron microscopy (TEM), using a Tecnai G₂ TF20 S-twin microscope (FEI Company). Prior to the observation of reduced samples, the catalyst was treated at 460 °C under H₂ for 4 h, which is similar to the reduction condition for the catalytic tests. The sample was then ultrasonically dispersed in ethanol and spread over a perforated copper grid. More than 300 nickel particles were counted to obtain the histograms of particle size distribution.

H₂-Temperature-Programmed-Reduction (H₂-TPR) measurements were performed using a TPD/R/O 1100 system (Thermo Scientific) equipped with a thermal conductivity detector (TCD). Before each TPR measurement, a 50 mg catalyst sample was outgassed in Ar at 200 °C for 1 h to remove impurities and then allowed to cool down to room temperature. For the TPR measurements, 50 mL min^{−1} of a 5% H₂/N₂ mixture was passed through the catalyst bed while the furnace temperature was increased at a rate of 10 °C min^{−1} from 50 °C to 900 °C.

NH₃-Temperature Programed Desorption (NH₃-TPD) was also conducted using TPD/R/O 1100 instrument. Before each NH₃-TPD measurement, 100 mg of catalyst was loaded into a quartz tube, was outgassed for 1 h in Ar at 200 °C, and then cooled down to 100 °C. After that, the outgassed catalyst was exposed to NH₃ for 1 h at a flowrate of 50 mL/min. Subsequently, the sample was flushed for 1 h under He at a flowrate of 50 mL min^{−1} to remove physisorbed molecules. For the TPD measurement, the catalyst was heated up with a ramp rate of 10 °C min^{−1} from 100 °C to 800 °C under He flow to desorb ammonia.

Fourier transform infrared (FTIR) spectroscopy was carried out on a BIO-RAD Excalibur series FTS 3000 spectrometer. For transmission FTIR studies, the sample was first mixed with KBr, ground thoroughly, and then pressed into a wafer for analysis. FTIR experiments either in the hydroxyl region or in the chemisorbed pyridine one (Pyr-IR) were conducted in a Bruker FTIR spectrometer (VERTEX 70) equipped with a Harrick Praying Mantis Diffuse reflectance Fourier transform infrared spectroscopy (DRIFTS) cell fitted with KBr windows, and connected to a gas flow system. Before DRIFT measurements, the samples were pretreated at 400 °C in He flow for 1 h. The FTIR spectra were recorded after cooling down to room temperature with a resolution of 4 cm^{−1}. Typically, 128 scans were recorded, averaged and transformed, employing Kubelka–Munk method. KBr was used as a reference to carry out background subtraction. For the Pyr-IR experiment, the pretreated sample was cooled down to room temperature and then exposed to pyridine vapor. The IR spectra of chemisorbed pyridine were recorded in the spectral range of 400–4000 cm^{−1} at a resolution of 4 cm^{−1}. The desorption of pyridine was carried out by heating the catalyst from room temperature to up to 400 °C and held at each temperature for half an hour. The collected spectra were normalized to the integrated area of Si–O overtones between 2100 and 1740 cm^{−1} of the activated sample.

X-ray photoelectron spectroscopy (XPS) was performed on a VG ESCALAB 250 spectrometer equipped with a monochromatic Mg K α radiation source. All binding energies were corrected using the peak position of C1s at 284.6 eV as a reference.

2.3. Catalytic measurements

All hydrogenolysis experiments were carried out in a 300 mL autoclave reactor (Parr Instrument). The feed, 5 wt% (THFA and THPM) or 1 wt% (125PTO, 15PDO, 126HTO, and 16HDO) in water, along with the appropriate amount of catalyst was loaded into the reactor and sealed. To remove air, the reactor was purged three times before pressurizing it with hydrogen to 500 psi. The pressurized vessel was then heated to the required temperature using a stirrer speed of 500 rpm for a given reaction time. At the end of the set reaction time, the reactor was cooled down to room temperature. The reactor was depressurized at room temperature, and the resultant products were then collected, weighed and subsequently centrifuged to separate liquid products from the catalyst. The liquid products were then filtered and transferred to vials while the solid catalyst was dried in a vacuum oven. Liquid products were quantitatively analyzed using an Agilent 6890 N gas chromatography (GC) and a Waters high performance liquid chromatography (HPLC). The GC was equipped with CPWAX 52 CB column and a flame ionization detector (FID). The HPLC was equipped with a Refractive Index Detector (RID) and an ion–exclusion column (Aminex HPX-87H, 300 mm × 7.8 mm), kept at 60 °C, with 0.005 M H₂SO₄ at a flowrate of 0.5 mL min^{−1} as the mobile phase. Inductively coupled plasma atomic emission spectrometry (ICP–AES) was used to detect the presence of Ni in reaction products.

2.4. Infrared spectroscopy of adsorbed THFA

DRIFT spectra of adsorbed THFA were recorded in a Bruker FTIR spectrometer (VERTEX 70) equipped with a Harrick DRIFTS cell. The Ni/ZSM-5 sample was loaded into the cell, reduced in-situ at 500 °C for 1 h under flowing H₂ (30 ml/min), cooled down to room temperature, and then purged with He (30 ml/min). For ZSM-5 zeolite, the sample was pretreated at 400 °C in He flow for 1 h. THFA vapor was then passed through the cell using a saturator at room temperature and either He or H₂ as carrier gas. The DRIFT spectra were recorded at room temperature for 1 h. The sample was purged under He flow at room temperature for another 30 min and then heated up to 400 °C with a heating rate of 10 °C min^{−1} under He or H₂ flow. The DRIFT spectra were recorded at room temperature after each step. Each spectrum is the result of an average of 128 scans in the spectral range of 400–4000 cm^{−1} at a resolution of 4 cm^{−1}.

2.5. Calculation of kinetic diameters of selected reactants and products

Kinetic diameters of the selected molecules were determined from the properties of the molecule at the critical point, using the following equation [29, 34]:

$$\sigma = 0.841 V_c^{1/3} \quad (1)$$

where V_c is the critical volume in cm³ mol^{−1}. The critical data were obtained from Joback et al. [35], and the CRC handbook of chemistry and physics [36]. The Joback method predicts the thermodynamic properties of the molecule based on its structure.

Eq. (2) was also used to estimate the kinetic diameters of molecules, assuming spherical molecule [29]:

$$\sigma = 1.234 M_w^{1/3} \quad (2)$$

where M_w is the molecular weight in g mol^{−1}. The estimated diameters determined from both Eqs. (1) and (2) are listed in Table 1.

3. Results

3.1. Characterization results

The physicochemical properties for the parent zeolites and Ni–zeolite catalysts are summarized in Table S2 (Supplementary

Table 1
Kinetic diameters of reactants, intermediates, and reaction products.

Molecule	V_c^a (cm ³ mol ⁻¹)	M_W (g mol ⁻¹)	σ (Å)	
			Eq. (1)	Eq. (2)
THFA	296.5	102.13	5.60	5.77
15PDO	353.5	104.15	5.94	5.81
125PTO	366.5	120.15	6.01	6.09
DHP	268.0 ^b	84.13	5.42	5.41
THP	263.0 ^b (270.5 ^a)	86.13	5.38 (5.43 ^c)	5.45
2-HTHP	288.5	102.13	5.55	5.77
THPM	344.5	116.16	5.89	6.02
126HTO	422.5	134.18	6.30	6.32
16HDO	409.5	118.18	6.24	6.06
OXE	301	100.16	5.63	5.73

^a Determined from Joback method [35].

^b Determined from CRC handbook [36].

^c Used V_c derived from Joback method.

Material) and Table 2, respectively. The Ni loading of the catalysts was fixed at about 10 wt%. The nickel loadings determined by XRF range from 9.2 wt% to 10.3 wt%, being the differences attributed to the differences in catalyst supports and preparation methods. The variation of the solution pH during D-P of Ni (II) species on ZSM-5 is shown in Fig. S1 (Supplementary Material). The solution pH starts at a value of about 2 and increases to a maximum value of around 5.7 due to the formation of OH⁻ ions by hydrolysis of urea at 90 °C. The pH curve then reaches a plateau at around 5.5 because of the dynamic equilibrium between the generation of OH⁻ ions and their consumption for D-P of Ni(II) species onto the support. The shape of pH variation curve is consistent with the trend reported in the literature during D-P of Ni on highly siliceous zeolite supports [21,23]. Similar trends with slight changes are observed for the other zeolite-supported Ni catalysts.

BET surface areas (S_{BET}), external (S_{ext}) and microporous (S_{micro}) surface areas, total pore volume ($V_{p,t}$), as well as mesoporous ($V_{p,meso}$) and microporous ($V_{p,micro}$) pore volumes of zeolite-supported Ni catalysts are also reported in Table 2. The BET surface areas of Ni/BETA and Ni/SAPO-34 are the highest, ca. 550 m² g⁻¹ and 470 m² g⁻¹, respectively, having also the highest external and microporous surface areas. Ni/MOR, Ni/ZSM-11 and Ni/ZSM-5 catalysts have intermediate BET surface areas (350–390 m² g⁻¹), while Ni/FER has the lowest BET surface area (290 m² g⁻¹). Ni/BETA zeolite possesses the highest total pore volume of 1 cm³ g⁻¹, while the total pore volume for the other catalysts range from 0.3 to 0.4 cm³ g⁻¹. Compared to Ni/ZSM-5 catalyst, the sample prepared by IWI method shows a decrease in BET surface area, microporous and mesoporous surface areas and pore

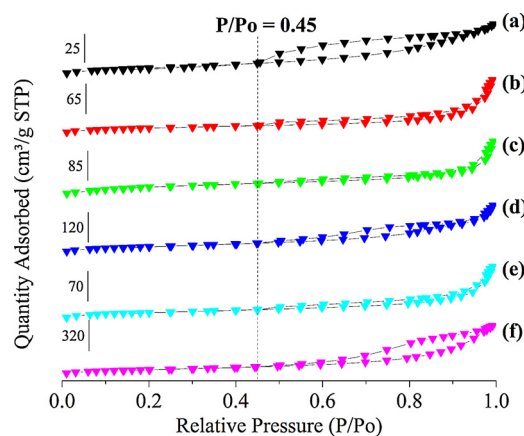


Fig. 1. N₂ Adsorption–Desorption isotherms: (a) Ni/SAPO-34, (b) Ni/FER, (c) Ni/ZSM-5, (d) Ni/ZSM-11, (e) Ni/MOR, and (f) Ni/BETA.

volumes.

The N₂ adsorption–desorption isotherms at −196 °C for all Ni–zeolite catalysts are shown in Fig. 1, while those of their corresponding zeolitic supports are presented in Fig. S2 in Supplementary Material. All zeolites except BETA present type I isotherms, which is characteristic of microporous materials. These zeolites also exhibit H₄ type hysteresis loops, having ZSM-11 the larger hysteresis loop, showing that it has a greater degree of mesopores as compared to other zeolites, in agreement with the values of mesoporous surface area and volume (Table S2). On the other hand, BETA zeolite shows a type IV adsorption–desorption isotherm with a very high uptake of N₂, indicating that it has the largest proportion of mesopores/porous ratio among all zeolites. The D-P process does not change the shape of the isotherms of the Ni–zeolites as compared to their parent zeolites. However, a shift towards an H₃ hysteresis loop at $P/P_0 > 0.45$ is noticed for Ni–zeolites, indicating the formation of mesopores during D-P process.

Fig. 2 shows the XRD patterns of the bare zeolites along with uncalcined, calcined and reduced Ni–zeolite catalysts. It is evident that for most catalysts prepared by D-P, the intense diffraction peaks at 2θ values between 20°–30°, corresponding to the zeolite structures, does not change significantly as compared to the parent zeolite. For Ni/ZSM-11, however, the characteristic peaks of the zeolite seem to be transformed into smaller broad peaks upon reduction step. This result indicates that the ZSM-11 zeolite structure may have been partly degraded after the reduction. This could result from the steam produced during the reduction process, which may contribute to degrade the

Table 2
Physicochemical Properties of zeolite-supported Ni nanoparticles.

Catalyst	Ni loading ^a (wt%)	S_{BET}^b (m ² g ⁻¹)	$S_{ext}^{b,c}$ (m ² g ⁻¹)	S_{micro}^c (m ² g ⁻¹)	$V_{p,t}^{b,d}$ (cm ³ g ⁻¹)	$V_{p,meso}^{b,e}$ (cm ³ g ⁻¹)	$V_{p,micro}^{b,c}$ (cm ³ g ⁻¹)	Acidity (μmol g ⁻¹)	
								Total ^f	BAS/LAS ^g
Ni/SAPO-34	9.3	467.7	36.2	431.5	0.3	0.09	0.21	2257.9	–
Ni/FER	9.4	288.3	61.3	227	0.3	0.19	0.11	2159.6	–
Ni/ZSM-5	10.3	346.8	153.6	193.2	0.34	0.25	0.09	1580.5	1.0
Ni/ZSM-11	9.2	357.4	145.1	212.3	0.39	0.3	0.09	1683.4	0.54
Ni/MOR	9.9	385.8	74.1	311.7	0.35	0.2	0.15	2507.5	2.2
Ni/BETA	9.7	556.2	287.6	268.6	1	0.87	0.13	2705.0	0.41
Ni/ZSM-5-IWI	10.0	317	120.3	196.7	0.23	0.13	0.1	1553.1	–

^a Determined by XRF.

^b Determined by BET method.

^c Determined by t-plot method.

^d Determined by single point adsorption.

^e Determined by BJH method.

^f Determined by NH₃-TPD.

^g Determined by Py-IR, Brønsted (BAS), Lewis (LAS) acid sites.

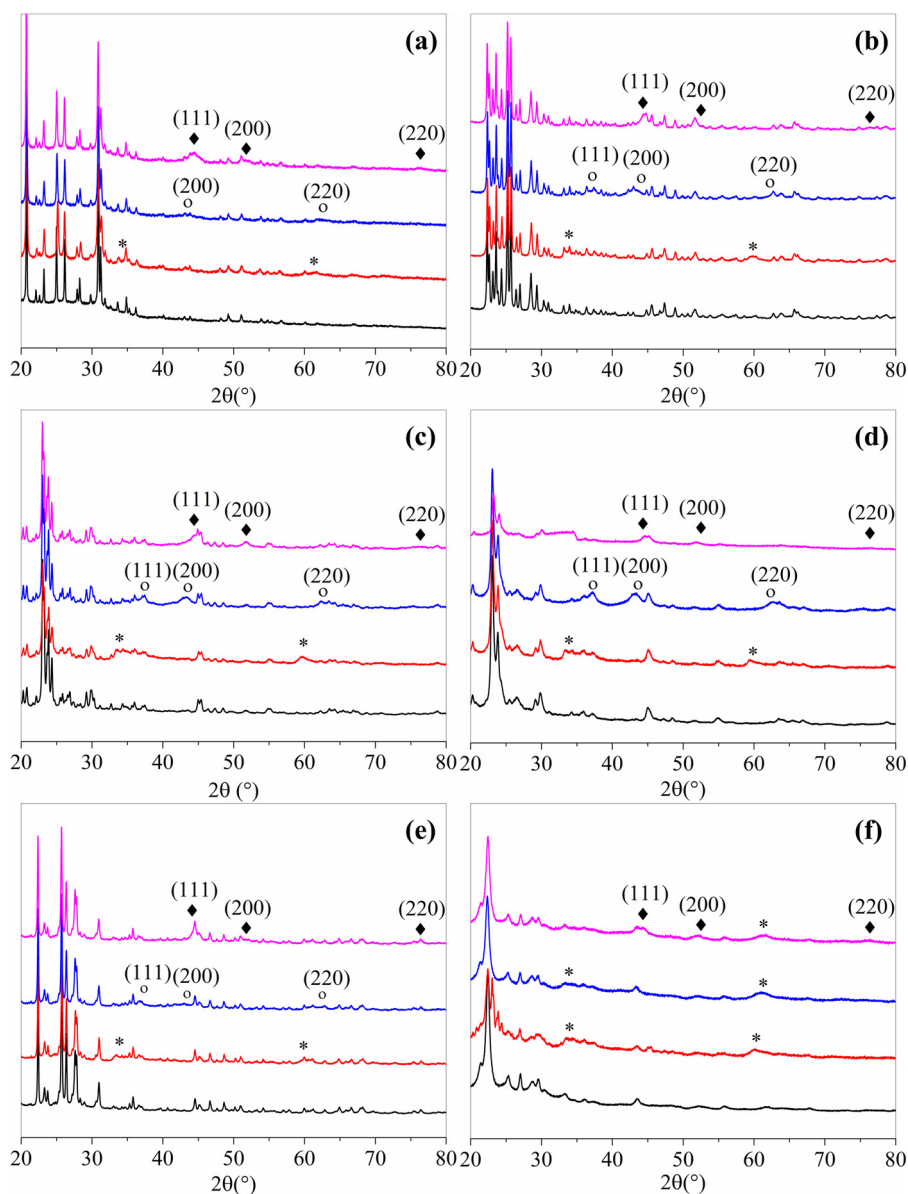


Fig. 2. XRD patterns of bare zeolites (black, 1st pattern from bottom), uncalcined (red, 2nd pattern from bottom), calcined (blue, 3rd pattern from bottom), and reduced (pink, top pattern) catalysts: (a) Ni/SAPO-34, (b) Ni/FER, (c) Ni/ZSM-5, (d) Ni/ZSM-11, (e) Ni/MOR, and (f) Ni/BETA. Peak identification: (*) Ni-phylllosilicate or $\text{Ni}(\text{OH})_2$, (○) NiO , and (◆) metallic Ni. (For interpretation of the references to colour in this figure legend, the reader is referred to the web version of this article).

structure of the ZSM-11 zeolite. For the uncalcined Ni catalysts, two new diffraction peaks appear at 20 of around 34° and 60° , which can be assigned either to nickel hydroxide or to ill-crystallized 1:1 nickel phyllosilicate species. However, it is difficult to discriminate between these two species due to the overlap of the other peaks with the characteristic peaks of the zeolites. Another set of broad reflections at $2\theta = 37^\circ$, 43° , and 63° , corresponding to the (111), (200), and (220) planes of NiO phase are also observed in XRD patterns of calcined catalysts, except for Ni/BETA catalyst. Similar characteristics peaks are also observed for Ni/ZSM-5-IWI as shown in Fig. S3 (Supplementary Material), though considerably larger NiO crystallite sizes (ca. 20 nm) are observed as compared to the ones of the catalyst prepared by D-P method. For calcined Ni/BETA catalyst, however, the peak at 34° is still detected along with the peak at 60.9° , which is slightly shifted to higher angles as compared to the uncalcined sample, indicating the possible presence of 2:1 Ni phyllosilicate phase [37]. The latter peak is still present in the XRD pattern of reduced Ni/BETA catalyst. Additionally, diffraction peaks at 44° (111), 52° (200) and 76° (220) are detected,

indicating the transformation of NiO and some Ni phyllosilicate into metallic Ni.

It was widely reported that catalysts prepared by D-P method can exhibit very small metal particles, as evidenced by the low intensity of rather broad peaks in the XRD patterns of Ni-zeolite catalysts. However, it is difficult to estimate Ni crystal size from the XRD patterns. Therefore, TEM was employed to determine catalyst morphology and Ni particle size distribution. As shown in the histograms of the Ni particle size distribution in Fig. 3, a range of particle sizes between 2 nm to 10 nm is obtained for all reduced Ni-zeolite catalysts. The mean Ni particle size is between 5.5 nm to 5.9 nm, with the smallest mean size of around 4.8 nm for Ni/MOR catalyst, in agreement with XRD data. Moreover, the TEM image of calcined Ni/ZSM-5 (Fig. S4, Supplementary Material) shows that the Ni lamellar structures (i.e., Ni phyllosilicate) are mainly distributed on the external surface of zeolite surface. These lamellar structures are still present in the TEM images of all reduced Ni-zeolite catalysts, mostly Ni/BETA catalyst, implying an incomplete reduction of the Ni phyllosilicates.

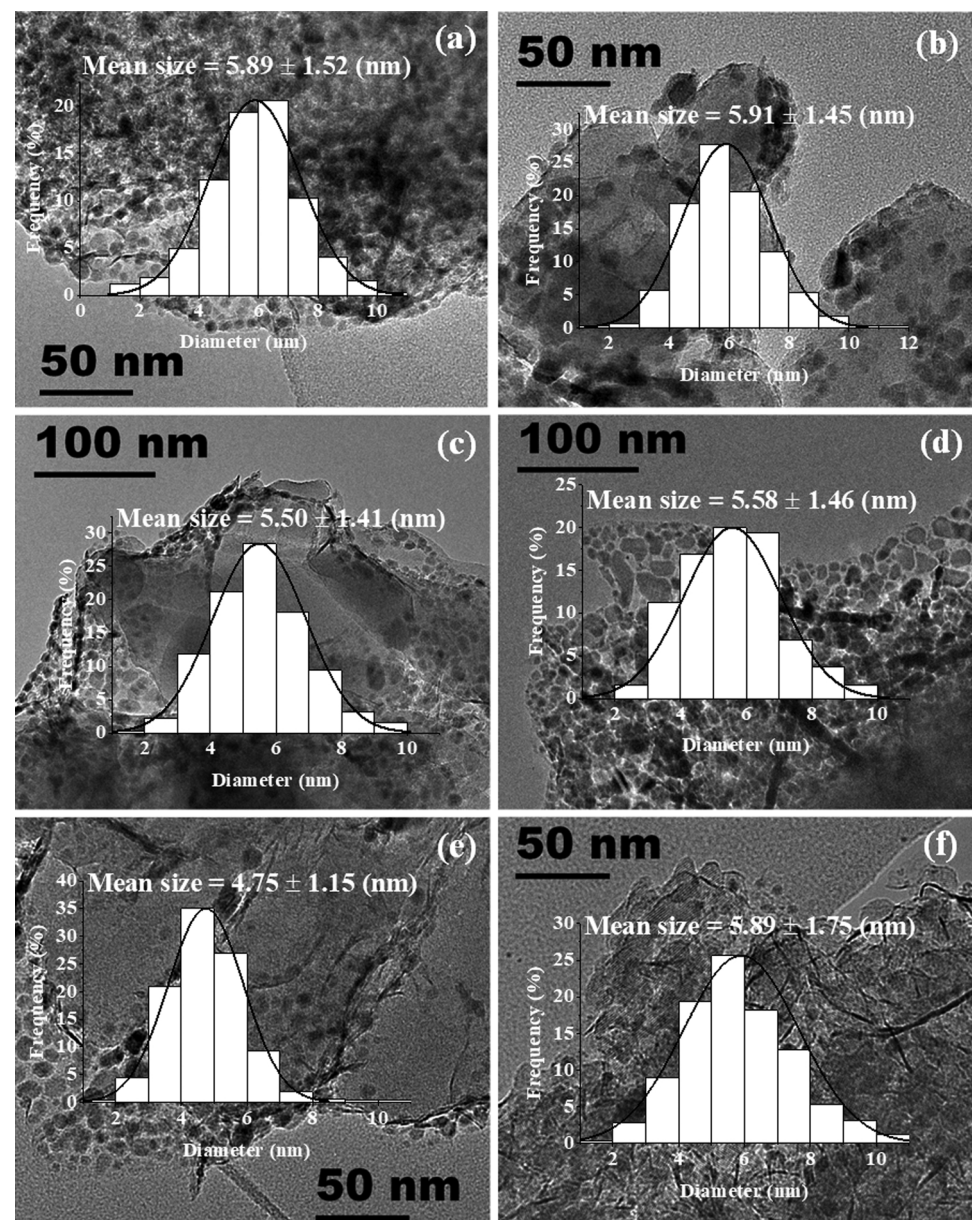


Fig. 3. TEM images of reduced catalysts: (a) Ni/SAPO-34, (b) Ni/FER, (c) Ni/ZSM-5, (d) Ni/ZSM-11, (e) Ni/MOR, and (f) Ni/BETA. The dark black dots in all images are nickel particles. The insets show the size distribution histograms of Ni particles (after counting around 300 particles).

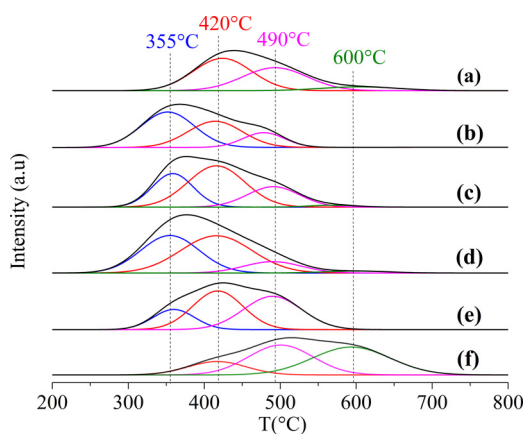


Fig. 4. H₂-TPR profiles of calcined catalysts: (a) Ni/SAPO-34, (b) Ni/FER, (c) Ni/ZSM-5, (d) Ni/ZSM-11, (e) Ni/MOR, and (f) Ni/BETA.

H₂-TPR measurement was then performed to explore the reducibility of the catalysts, and the TPR profiles are shown in Fig. 4. Ni/SAPO-34 catalyst reduction (Fig. 4(a)) begins at approximately 300 °C with two major peaks centered at around 420 °C and 490 °C, coupled with a low-intensity shoulder at higher temperature (around 600 °C). The first peak corresponds to the reduction of supported NiO particles, while the second one can be attributed to the reduction of 1:1 Ni phyllosilicate structure. The latter shoulder peak could therefore be assigned to the reduction of 2:1 Ni phyllosilicate with stronger metal-support interaction [22,38]. The TPR profiles derived for Ni/FER, Ni/ZSM-5, Ni/ZSM-11, and Ni/MOR catalysts in Fig. 4(b)–(e) can be deconvoluted into three peaks with different relative proportions, as reported in Table S3 (Supplementary Material). The first peak at the lowest temperature (i.e., 355 °C) can be assigned to the reduction of NiO species with weak interaction with the support, which are generated from the decomposition of nickel hydroxide. Pure NiO typically shows a single TPR peak between 300 °C to 400 °C [39]. Like Ni/SAPO-34 catalyst, the higher-temperature peaks at around 420 °C and

490 °C are characteristics of supported NiO and 1:1 Ni phyllosilicate species, respectively. It should be mentioned that no detectable 1:1 Ni phyllosilicate diffraction peaks are observed in the XRD patterns of calcined catalysts, which might be due to the high dispersion of 1:1 phyllosilicate on the surface of these catalysts. Finally, Ni/BETA catalyst (Fig. 4(f)) exhibits a much broader hydrogen consumption profile from 300 °C to 750 °C, with three maxima centered at 420 °C, 490 °C, and 600 °C. As compared to the other Ni-zeolite catalysts, Ni/BETA catalyst has a higher concentration of 2:1 Ni phyllosilicate, which is consistent with XRD data. For Ni/ZSM-5-IWI catalyst (Fig. S5, Supplementary Material), three reduction peaks at around 390 °C, 420 °C and 480 °C are observed, resulting in lower hydrogen consumption of around 693 μmol g⁻¹, as compared to that of Ni/ZSM-5 catalyst (796 μmol g⁻¹). Moreover, the reduction peak at 480 °C can be assigned to the reduction of smaller nickel oxide crystallites, which has a strong interaction with the HZSM-5 support.

The transmission FTIR spectra of bare zeolites, uncalcined, and calcined Ni-zeolites catalysts are reported in Fig. S6 (See Supplementary Material for detailed band assignments). All spectra show the characteristic bands of zeolites framework at around 440–470, 520–600, 795–810, 1083–1097 and 1222 cm⁻¹. The band at 634–638 cm⁻¹, a characteristic band of the δ_{OH} vibration mode of nickel hydroxide, appears for all uncalcined Ni-zeolite catalysts. Two bands at 663–667 and 975 cm⁻¹ also appear in the spectra of uncalcined catalysts, which can be assigned to the tetrahedral Si–O mode and Si–O stretching of 1:1 nickel phyllosilicate ($\text{Ni}_3\text{Si}_2\text{O}_5(\text{OH})_4$), respectively. Moreover, band at 875–877 cm⁻¹ is detected for some uncalcined samples, indicating the presence of the poorly crystallized nickel phyllosilicate on the surface of the catalysts [22]. Compared to the uncalcined catalysts, the band at around 637 cm⁻¹ disappears, indicating the decomposition of nickel hydroxide in the calcined catalysts. It should be mentioned that the band at around 480 cm⁻¹, corresponding to Ni–O stretching vibration, cannot be observed in the calcined catalysts due to the strong zeolites bands at 440–470 cm⁻¹. Additionally, the vibration bands of nickel phyllosilicates are very close to those of bare zeolites, which makes the interpretation difficult. Thereby, ZSM-5 support, as an example, was treated in the D-P process without nickel nitrate, as described in the materials and methods section. The calcined Ni/ZSM-5 spectrum was then subtracted from the urea-treated ZSM-5 spectrum (Fig. S7 of Supplementary Material). The bands at around 663 cm⁻¹ and 862 cm⁻¹ further supports the presence of 1:1 nickel phyllosilicate in the calcined catalysts. Finally, according to the previous studies [22,38], the bands at around 670 and 710 cm⁻¹ could be attributed to tetrahedral Si–O mode and δ(OH) vibration of isolated hydroxyls surrounded by three nickel atoms of 2:1 nickel phyllosilicate ($\text{Ni}_3\text{Si}_4\text{O}_{10}(\text{OH})_2$), respectively. Therefore, the band at 700 cm⁻¹ in the FTIR spectrum of calcined Ni/BETA catalyst can be attributed to the presence of 2:1 nickel phyllosilicate species, in good agreement with XRD and TPR results.

FTIR spectra in the hydroxyl region (3000–4000 cm⁻¹) over bare zeolites along with the uncalcined and calcined catalysts are shown in Fig. S8 (See Supplementary Material for detailed band assignments). The spectra obtained for all parent zeolites exhibit the band at around 3743–3747 cm⁻¹ which can be assigned to the ν(OH) vibrational mode of the terminal Si–OH groups in the external surface of the zeolite. The band at around 3600–3613 cm⁻¹ can be ascribed to bridging hydroxyls Si–OH–Al groups, indicating the presence of strong Brønsted acid sites [40]. For Ni-zeolites catalysts, the band intensity at 3743–3747 cm⁻¹ remains nearly unchanged after the D-P process, with only a slight shift to lower wavenumbers, especially for uncalcined Ni catalysts. It is evident that a new band centered at 3700–3708 cm⁻¹ is observed for all uncalcined catalysts except Ni/SAPO-34, as shown in Fig. S8(b)–(f). Notably, this band is also present in the bare ZSM-5. Previous studies found that ZSM-5 zeolite contains “hydroxyl nests”, a cluster consisting of four internal Si–OH groups, which can be aggregated to form hydroxylated nanocavities [22]. The band at 3680–3686 cm⁻¹ (more

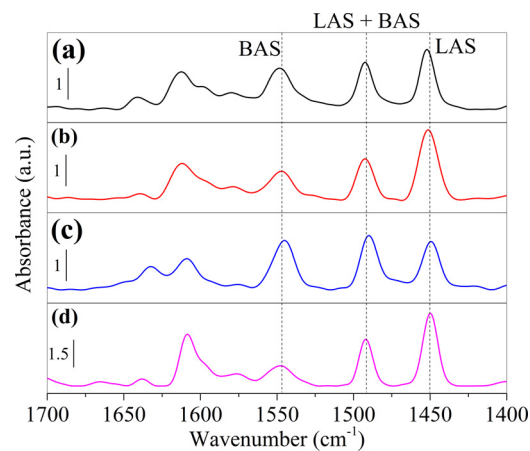


Fig. 5. FT-IR spectra of adsorbed pyridine over calcined catalysts after desorption at 200 °C: (a) Ni/ZSM-5, (b) Ni/ZSM-11, (c) Ni/MOR, and (d) Ni/BETA. BAS: Brønsted acid sites, LAS: Lewis acid sites.

obvious in Ni/FER and Ni/ZSM-11 spectra) is typically assigned to OH-groups attached to extra-framework T atom-containing species [40]. Thus, it can be concluded that this band corresponds to the absorption of surface hydroxyls in 1:1 nickel phyllosilicate. Additionally, another band at around 3647–3657 cm⁻¹ can be attributed to the integrated absorption of surface hydroxyls in nickel hydroxide and 1:1 nickel phyllosilicate [22], while the band at around 3500–3580 cm⁻¹ is ascribed to the vibration of OH group attached to multivalent cations (i.e., nickel hydroxide) [22,40]. For calcined Ni/BETA catalyst, the weak absorption peak at around 3622 cm⁻¹ can be attributed to the stretching of ν(OH) band of 2:1 nickel phyllosilicate structure, supporting previous findings by FTIR, H₂-TPR, and XRD.

Acid properties of Ni-zeolite catalysts were measured by FTIR of adsorbed pyridine and TPD of NH₃. FTIR spectra of adsorbed pyridine over calcined Ni-zeolite catalysts are presented in Fig. 5, along with the molar ratio of Brønsted to Lewis acid sites (BAS/LAS) listed in Table 2. It should be noted that SAPO-34 and FER zeolites cannot be probed by pyridine adsorption because their small pore sizes (Table S1) do not allow pyridine molecule (5.7 Å) to reach all internal acid sites. Therefore, ammonia (2.6 Å) was employed as a probe molecule to access both Lewis and Brønsted acid sites, and the total acid amounts determined from NH₃-TPD experiments were quantified and are reported in Table 2. The largest amount of acid sites is observed for Ni/BETA and Ni/MOR with 2700 and 2500 μmol g⁻¹, respectively. Ni/SAPO-34 and Ni/FER catalysts possess an intermediate concentration of acid sites (i.e., approximately 2200 μmol g⁻¹), while the lowest amount of acid sites of around 1600 μmol g⁻¹ is observed for both Ni/ZSM-5 and Ni/ZSM-11 catalysts. Compared to the bare zeolites (Table S2 of Supplementary Material), the amount of total acid is increased after Ni loading during the D-P process, suggesting generation of high concentration of Lewis acidity due to Ni²⁺ [41]. For Ni/ZSM-5-IWI catalyst, the total concentration of acid sites is slightly lower than Ni/ZSM-5 catalyst, which could be due to the increasing amount of acidic OH groups of nickel phyllosilicate species in the sample obtained by D-P method.

As shown in Fig. 5, the IR bands appeared at around 1450 cm⁻¹ and 1545 cm⁻¹ are ascribed to the adsorption of pyridine on Lewis and Brønsted acid sites, respectively, while the band near 1490 cm⁻¹ is due to the presence of both Brønsted and Lewis acid sites. The ratio of Brønsted to Lewis acid sites were determined from the integration of IR band at 1450 cm⁻¹ and 1545 cm⁻¹, employing molar extinction coefficients of 1.23 and 1.73 cm μmol⁻¹ for Brønsted and Lewis acid sites, respectively [42]. As shown in Table 2, it can be seen that Ni/MOR has the highest BAS/LAS ratio of around 2.2, indicating the dominant concentration of Brønsted acid sites in mordenite, regardless of decreasing density of Brønsted acidity after incorporation of nickel.

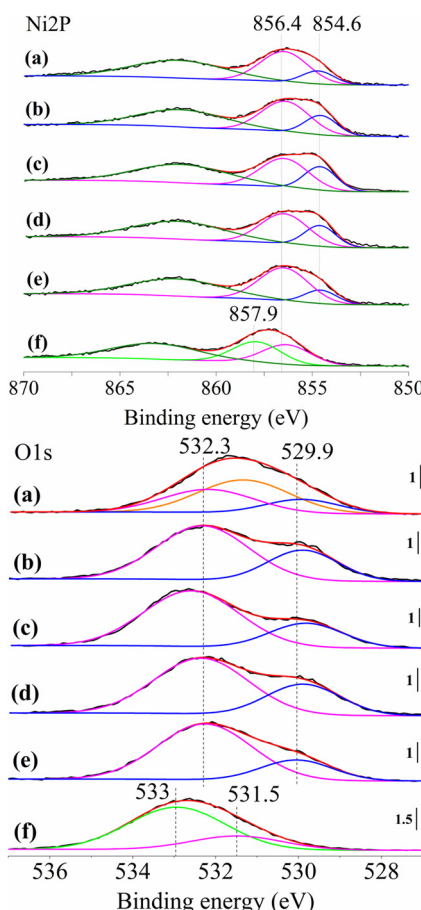


Fig. 6. Ni2p and O1s XPS spectra of calcined catalysts: (a) Ni/SAPO-34, (b) Ni/FER, (c) Ni/ZSM-5, (d) Ni/ZSM-11, (e) Ni/MOR, and (f) Ni/BETA.

Additionally, Ni/ZSM-5 catalyst exhibits similar Brønsted and Lewis site densities, while BAS/LAS ratios of around 0.54 and 0.41 are observed for Ni/ZSM-11 and Ni/BETA catalysts, respectively.

To further understand the structural variations of surface species, XPS measurements were carried out on calcined Ni-zeolite catalysts. Fig. 6 shows the Ni2p and O1s XPS spectra of calcined Ni-zeolite

catalysts, while XPS parameters of the Ni2p, O1s, and Si2p peaks in zeolite-supported Ni nanoparticles are listed in Table S4 (Supplementary Material). As shown in Fig. 6(a)–(e), Ni2p_{3/2} spectra of calcined catalysts can be deconvoluted to two-component peaks with binding energies of 854.6 eV and 856.4 eV with different ratios for the different Ni-zeolite catalysts. The former peak is characteristic of Ni²⁺2p_{3/2} of NiO species on the surface of the calcined catalyst [43]. The latter one can be assigned to the Ni²⁺2p_{3/2} of 1:1 Ni phyllosilicate species [43]. For Ni/BETA catalyst, no obvious signals corresponded to NiO species are identified, whereas a new peak at 857.9 eV can be ascribed to the Ni²⁺2p_{3/2} of 2:1 Ni phyllosilicate species [43]. Similarly, the peak fittings for O1s spectra of all Ni-zeolites, except for Ni/BETA, consist of two peaks with binding energies of 529.9 eV and 532.3 eV, assigned respectively to oxygen ions in NiO and 1:1 Ni phyllosilicate species [43]. It is important to note that another peak is observed in the O1s spectrum of Ni/SAPO-34 catalyst, which is probably due to oxygen ions in Al₂O₃ and P₂O₅ species. Two peaks at binding energies of 531.5 and 533 eV are identified for Ni/BETA sample, which can be assigned to the 1:1 Ni phyllosilicate and 2:1 Ni phyllosilicate species, respectively. In addition, the difference between Ni2p_{3/2} and Si2p ($\Delta_{\text{Ni-Si}}$) has been used to further support these findings derived from Ni2p and O1s spectra and the results are listed in Table S4 (Supplementary Material). According to previous studies [43], $\Delta_{\text{Ni-Si}}$ values in the range of 752.8–753.8 eV are attributed to nickel silicates, while other Ni species exhibit smaller binding energy separation [43]. This result further indicates the presence Ni phyllosilicate species on the surface of calcined Ni-zeolite catalysts.

3.2. Catalytic results

3.2.1. Hydrogenolysis of THFA

The results of catalytic tests over zeolite-supported nickel catalysts, along with those over some parent zeolites are presented in Table 3. For all Ni-zeolite catalysts (entry 1–8), the ring-opening reaction occurs at the more sterically hindered secondary C–O bond, yielding mainly 15PDO, 125PTO and THP. Other products, including 3-hydroxytetrahydropyran (3-HTHP), 2-methyltetrahydrofuran (2-MTHF), tetrahydrofuran (THF), and 1-butanol, are labeled as “others” in Table 3. It is evident that the catalytic performance of the Ni catalysts prepared by D-P method strongly depends on the nature zeolite used as support. The highest THFA conversion of around 91–93% is observed over Ni/ZSM-5 and Ni/ZSM-11 catalyst, followed by an intermediate

Table 3
C–O bond Hydrogenolysis of THFA over zeolite-supported Ni nanoparticles.

Entry	Catalyst	Conversion (%)	Product selectivity (%)					Rate ($\mu\text{mol gcat}^{-1} \text{min}^{-1}$)
			15PDO	125PTO	THP	2-HTHP	others ^a	
1	Ni/SAPO-34	6.2	25.9	48.7	2.1	4.8	3.8	26
2	Ni/FER	35.5	31.1	11.3	19.7	0.1	15.9	143.6
3	Ni/ZSM-5	92.9	3.7	0.2	68.4	0.1	7.2	385.0
4	Ni/ZSM-11	91.1	4.8	1.4	64.6	0.4	6.8	350.2
5	Ni/MOR	13.1	38.4	19.7	9.1	2	12.7	52.4
6	Ni/BETA	28.8	27.5	7.9	28.4	1.1	12.4	118.1
7	Ni/ZSM-5 ^b	35.2	33.9	12.4	22.7	0.1	8.9	2279.9
8	Ni/ZSM-11 ^b	32.8	33	13.6	24.9	0.1	9.7	2167.5
9	ZSM-5	39.5	4.1	10	2.4	26.9	4.9	162.9
10	BETA	33	3.9	12.2	4	10.9	5	135.5
11	Ni/BETA ^c	25.9	17.9	9.5	18.1	5.1	13.1	107.2
12	Ni/ZSM-5-IWI ^d	79.2	8.5	2.5	54.8	0	9.2	322.2
13	Ni/ZSM-5 ^e	74.3	12.4	3	49.4	0.5	9.5	296.1

Reaction conditions: 250 °C, 500 psi H₂, 4 h, 5 wt % THFA in water (100 g), 0.5 g catalyst.

^a Others include 1-pentanol, 3-HTHP, 2-MTHF, THF, and 1-butanol.

^b 15 min reaction.

^c Reduced at 600 °C for 2 h.

^d Catalyst prepared by incipient wetness impregnation (IWI) method.

^e 2nd run.

conversion level in the range of 30–36% on Ni/FER and Ni/BETA catalysts. Ni/SAPO-34 and Ni/MOR catalysts show much lower activities (i.e., around 6% and 13%, respectively), as compared to the other zeolite-supported nickel catalysts.

C–O hydrogenolysis reaction is a complex reaction, thereby the reaction rate could be affected by various parameters including Ni active sites, zeolite pore structure, zeolite acidity, as well as the reactant and product diffusion rates inside the zeolite pores. Comparing the reaction rates over different Ni–zeolite catalysts, it is evident that either one of the abovementioned parameters or their integrated effects can play a crucial role in THFA ring-opening reaction. To have a better insight into the shape selectivity of zeolites on the product distribution [28], ZSM-5- and ZSM-11-supported Ni catalysts were employed in THFA hydrogenolysis at shorter reaction time (i.e., 15 min) to achieve lower conversion levels, as reported in Table 3, entry 7 and 8. It is clear that at a conversion level of around 30%, nearly comparable product distribution of 15PDO (~27–34%), THP (~20–28%), and 125PTO (~8–14%) is observed. However, the highest 15PDO and 125PTO selectivity of around 38% and 49% are respectively achieved over Ni/MOR and Ni/SAPO-34 catalysts, while THFA conversion level is considerably lower as compared to other catalysts. This data implies that zeolite pore structure may not significantly affect the product distribution in THFA hydrogenolysis.

To better understand the role of Ni and other Ni species (i.e., Ni phyllosilicate), the C–O hydrogenolysis reaction over bare ZSM-5 and BETA zeolites was studied, and the results are presented in Table 3, entry 9 and 10, respectively. As compared to Ni/ZSM-5 (entry 3), significantly lower THFA conversion is achieved over bare ZSM-5, indicating the crucial role of nickel species on the C–O cleavage pathway. 2-HTHP with a selectivity of around 27% is obtained as a major product, followed by 125PTO (10%), while only 4% 15PDO is produced over ZSM-5 catalyst. As mentioned in the introduction, an indirect ring-opening pathway in THFA hydrogenolysis reaction exists [12,13,44]. In the absence of hydrogenation sites over bare zeolite, the latter step (i.e., ring-opening tautomerization and hydrogenation) is strongly inhibited. Likewise, a similar trend is observed for BETA zeolite, with a slight enhancement in THFA conversion as compared to BETA-supported Ni catalyst. For both zeolites, the sum of all products is remarkably lower (< 50%), clearly indicating the impact of bi-functional catalysts in inhibiting condensation reactions.

According to the characterization results, Ni/BETA catalyst reduces at the highest temperature due to the presence of 2:1 Ni phyllosilicate structure. Therefore, we have explored the effect of reduction temperature (at 600 °C) in C–O bond cleavage of THFA under the same reaction conditions. As shown in Table 3 (entry 11), lower THFA conversion and lower selectivity towards 15PDO and THP are observed as compared to the values obtained over Ni/BETA catalyst reduced at 460 °C. Interestingly, a yellow-colored solution was observed, as shown in Fig. S9 (Supplementary Material), which could be due to humin formation via condensation reactions. This suggests that large pore structure in the vicinity of metallic nickel can facilitate side reactions.

The effect of catalyst preparation was subsequently studied by comparing the catalytic performance of Ni/ZSM-5 catalysts prepared by D-P and IWI methods, respectively. As shown in Table 3 (entry 12), THFA conversion and THP selectivity over Ni/ZSM-5-IWI catalyst decrease to 79% and 55%, respectively, as compared to those values obtained for Ni/ZSM-5 catalyst prepared by D-P method (93% conversion and 68% selectivity). Furthermore, C–O bond hydrogenolysis of THFA over Ni/ZSM-5 catalyst was investigated as a function of reaction time, and the results are presented in Fig. 7. As expected, 125PTO and 15PDO are initially formed through hydrolysis and hydrogenolysis pathway over Ni/ZSM-5 catalyst. In the meantime, THP can be produced via a cyclo-dehydration pathway at beginning of the reaction. THFA conversion and selectivity towards THP progressively increase up to ca. 64% THP yield, while pentane polyols selectivity remarkably decreases, particularly in the first hour of the reaction.

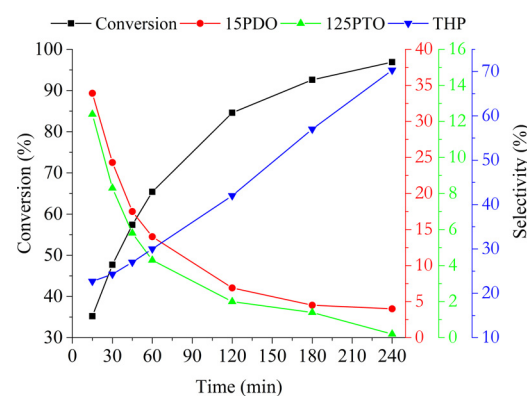


Fig. 7. Product distributions on THFA hydrogenolysis over ZSM-5-supported Ni nanoparticles as a function of reaction time. Reaction conditions: 250 °C, 500 psi H₂, 5 wt % THFA in water (100 g). Others include 3-HTHP, 2-MTHF, THF, and 1-butanol (not shown here).

3.2.2. DRIFT study of THFA adsorption on Ni/ZSM-5 catalysts

Ni/ZSM-5 catalysts were characterized by in-situ DRIFT spectroscopy after exposure to THFA in the presence of He or H₂ to elucidate the nature of surface species during the adsorption of THFA. The DRIFT spectra of adsorbed THFA on ZSM-5 and Ni/ZSM-5 samples using He as carrier gas are shown in Fig. S10. It is evident that the intensity of the Si–OH groups at around 3740 cm⁻¹ decreases due to the interaction of silanol groups with THFA. The bands in the range of 3500–3700 cm⁻¹ disappear while a new broad band at 3530 cm⁻¹ is observed, which can be attributed to the hydrogen-bonded O–H group [45]. Higher intensity of the bands at 2980 cm⁻¹, 2945 cm⁻¹ and 2880 cm⁻¹ is observed, being these bands characteristic of C–H stretching vibration modes of $\nu_{\text{asym}}(\text{CH}_3)$, $\nu_{\text{asym}}(\text{CH}_2)$ and $\nu_{\text{sym}}(\text{CH}_2)$, respectively [46]. This indicates the presence of physisorbed or weakly chemisorbed THFA on the surface of the catalysts. No bands corresponding to C–O stretching modes in the range of 1000–1100 cm⁻¹ are detected for both samples after exposure to THFA. It is also important to mention that the adsorption of THFA on Ni cannot be clearly observed due to the strong interaction between THFA and ZSM-5 structure. Moreover, the bands between 3500 and 3740 cm⁻¹ can be recovered by heating the samples up to 400 °C.

Fig. S11 shows the spectra collected when THFA flowed at room temperature on the Ni/ZSM-5 catalyst using H₂ as carrier gas. All bands previously observed in Fig. S10 are also present under flowing H₂. It must be stressed that a new band at around 3610 is observed after heating the catalyst to 400 °C, corresponding to the vibration mode of free O–H group (3600–3650 cm⁻¹). This may suggest the formation of ring-opening polyol products due to THFA transformation in the presence of H₂. However, a more reliable in-situ attenuated total reflection infrared (ATR-IR) spectroscopy is required to get more insight into the reaction mechanism [46].

3.2.3. Hydrogenolysis/dehydration of pentane polyols

To understand the effect of the zeolite structure on selectivity, we further explored the hydrogenolysis pathway starting from the reaction intermediates (i.e., 125PTO and 15PDO) over selected Ni–zeolite catalysts, and the results are presented in Tables 4 and 5, respectively. As reported in our previous study [15], 125PTO dehydration can proceed in high-temperature water and in the absence of a catalyst, resulting in a conversion of 32.8%. More importantly, the formation of five-membered cyclic ethers (55.8% THFA) is more favorable than the formation of six-membered ones (ca. 3% 3-HTHP). Similarly, as shown in Table 4, THFA is the main compound produced from cyclo-dehydration of 125PTO over different Ni–zeolite catalysts. The highest catalytic activity (> 90% conversion) is obtained over Ni/ZSM-5 catalyst, which is almost two times the one observed on the other Ni–zeolite catalysts

Table 4

C–O bond Hydrogenolysis of 125PTO over zeolite-supported Ni nanoparticles.

Catalyst	Conversion (%)	Product selectivity (%)				
		15PDO	THFA	THP	3-HTHP	others ^a
Ni/SAPO-34	45.1	6.3	76.8	1.1	2.1	6.4
Ni/FER	45.7	14.7	77.9	—	2.7	5.5
Ni/ZSM-5	92.4	12.3	66.8	5.8	1.5	2.6
Ni/BETA	38.0	7.8	68.7	—	2.7	3.9

Reaction conditions: 250 °C, 500 psi H₂, 4 h, 1 wt % 125PTO in water (100 g), 0.1 g catalyst.

^a Others include 1-pentanol, and 2-HTHP.

Table 5

C–O bond Hydrogenolysis of 15PDO over zeolite-supported Ni nanoparticles.

Catalyst	Conversion (%)	Product selectivity (%)		
		THP	1-pentanol	2-HTHP
Ni/FER	13.2	48.6	8.3	3.3
Ni/ZSM-5	53.3	88.9	3.7	—
Ni/MOR	10.4	44.8	3.1	4.3
Ni/BETA	6.0	26.4	—	6.4

Reaction conditions: 250 °C, 500 psi H₂, 4 h, 1 wt % 15PDO in water (100 g), 0.1 g catalyst.

tested in this reaction. Despite that, a comparable THFA selectivity of around 70% is achieved for all Ni–zeolite catalysts. In the case of Ni/SAPO-34 and Ni/FER catalysts, it seems that the 8-membered ring pores in the SAPO-34 and FER structures significantly inhibit the diffusion rate and the ring–closure pathway predominantly occurs on the external catalyst surface, leading to lower reaction rates as compared to ZSM-5, a medium pore size zeolite. For medium and large pores, it is expected that both internal and external active sites contribute to the dehydration pathway, yielding high conversion of 125PTO towards cyclic ether compounds. However, though Ni/BETA catalyst possesses the largest pore size and the highest concentration of acid sites, the lowest catalytic activity is obtained, which might be due to the participation of produced THFA in hydrolysis pathways towards 125PTO. Besides, higher THP yield is obtained over Ni/ZSM-5 catalyst, clearly promoting the subsequent dehydration of both THFA and 125PTO into THP.

A similar trend is observed for the hydrogenolysis of 15PDO, as shown in **Table 5**. 15PDO undergoes ring–closure pathway to form THP as a major product over all tested Ni–zeolite catalysts. Besides, 1-pentanol is produced through C–O hydrogenolysis. Ni/ZSM-5 shows remarkably higher conversion level and selectivity towards THP (i.e., around 53% conversion and 89% THP selectivity), as compared to the other Ni–zeolite catalysts. Likewise, the reaction over large pore MOR and BETA zeolites-supported Ni catalysts does not exhibit good catalytic performance for 15PDO dehydration into THP.

3.2.4. Hydrogenolysis of THPM to 16HDO

To obtain further insights into the effect of the zeolite topological structures, we have also examined the C–O bond hydrogenolysis of another cyclic ether, THPM, over nickel supported on medium and large pore zeolites. The THPM conversion and products distribution are shown in **Fig. 8**. It is evident that Ni supported on ZSM-5 and ZSM-11 are the most active catalysts in THPM ring-opening reactions. However, lower catalytic activity is obtained for all Ni–zeolite catalysts as compared to the conversion levels in THFA hydrogenolysis. This finding is in good agreement with previous studies, suggesting lower reactivity of six-membered ring molecules than four- and five-membered ones [8]. Considering product selectivity, it is obvious that THPM ring-opening can proceed at the most substituted carbon center, yielding 16HDO as the main product. In order to obtain lower conversion level over Ni/

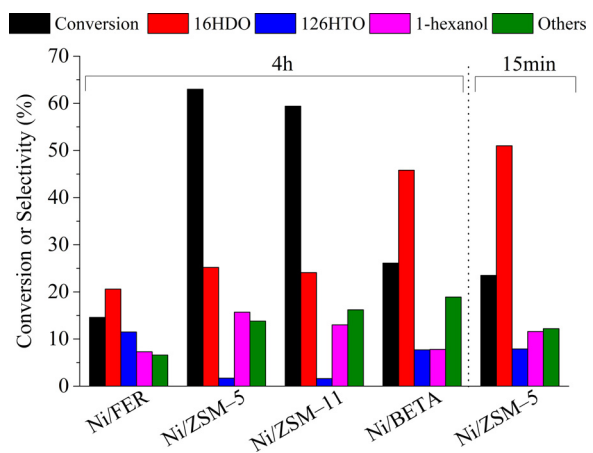


Fig. 8. C–O bond Hydrogenolysis of THPM over zeolite-supported Ni nanoparticles. Reaction conditions: 250 °C, 500 psi H₂, 5 wt % THPM in water (100 g), 0.5 g catalyst. Others include 12HDO, 15HDO, 3-HOXE, 2-MTHP, OXE, THP, 1-pentanol.

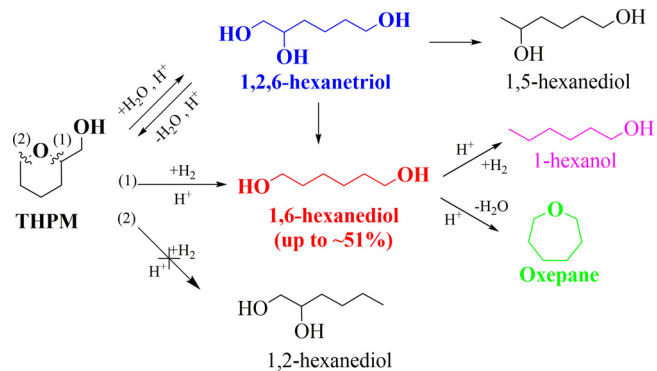


Fig. 9. Overall reaction pathways for the ring-opening of THPM under aqueous-phase conditions at 250 °C.

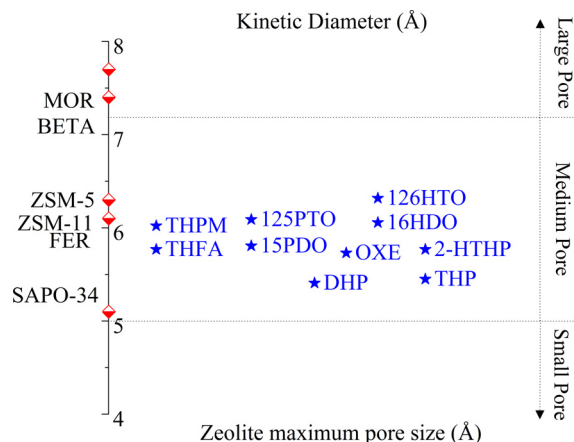
ZSM-5 catalyst, 15 min reaction time was employed while other reaction parameters were maintained constant. As shown in **Fig. 8**, the highest 16HDO selectivity of 51% is obtained over Ni/ZSM-5 catalyst, followed by 46% on Ni/BETA catalyst, at a THPM conversion level of around 25%. The major by-product is 1-hexanol, which can be produced via over-hydrogenolysis of 16HDO. Notably, 16HDO conversion by cyclo–dehydration pathway to produce oxepane (OXE) is remarkably lower than 15PDO ring–closure towards THP formation. It could be because of the higher stability of C₆ diol molecule or the lack of suitable active centers within the zeolite pores of the Ni–zeolite catalysts to efficiently promote ring–closure. Furthermore, THPM hydrogenolysis can proceed through protonation and S_N2-type reaction with water, producing 1,2,6-hexanetriol (126HTO), resulting in a selectivity lower than 10%. Various by-products including 1,2-hexanediol (12HDO), 1,5-hexanediol (15HDO), 3-hydroxyoxepane (3-HOXE), 2-methyltetrahydropyran (2-MTHP), THP, and 1-pentanol are also identified and reported as “others” in **Fig. 8**.

Eventually, we explored the catalytic activity of Ni/ZSM-5 in the hydrogenolysis/dehydration of C₆ polyols (i.e., 126HTO and 16HDO), and the results are reported in **Table 6**. Interestingly, unlike G₅ polyols, the hydrogenolysis pathway is significantly favored as compared to the dehydration route to produce cyclic ethers. For 126HTO hydrogenolysis, only 32.5% selectivity towards THPM is achieved via cyclo–dehydration pathways, while 16HDO (45.7%) and 15HDO (3.1%) are obtained at 59.1% 126HTO conversion level. No 12HDO is detected under these reaction conditions. This is consistent with the previous study by Buntara et al. [11], reporting the highest 16HDO selectivity of 73%, along with 15PDO at 17% 126HTO conversion level using

Table 6

C–O bond Hydrogenolysis of 126HTO and 16HDO over Ni/ZSM-5 catalyst.

Reactant	Conversion (%)	Product selectivity (%)					
		16HDO	15HDO	THPM	1-hexanol	OXE	Others
126HTO	59.1	45.7	3.1	32.5	4.5	0.9	6.8 ^a
16HDO	15.9	—	—	—	43.6	17	10.6 ^b

Reaction conditions: 250 °C, 500 psi H₂, 4 h, 1 wt % reactant in water (100 g), 0.1 g catalyst.^a Others include 3-HOXE, 2-MTHP-THP, 1-pentanol.^b 1-pentanol.**Fig. 10.** Kinetic diameters of cyclic ethers and polyols vs. zeolites maximum pore size.

Rh–ReO_x/SiO₂ catalyst. After addition of Brønsted acids as promoter, THPM was formed at very high yields. [11] Additionally, Dumescic et al. reported very high 16HDO selectivity (> 99%) at low 126HTO conversion level (8%) over Rh–ReO_x/C catalyst, while the 16HDO selectivity dropped to 61% at higher conversion level (59%) [8]. 1-hexanol (43.6%) is the major product obtained in the hydrogenolysis of 16HDO, followed by OXE (17%), at a remarkably low conversion level of 15.9%. Based on the experimental results, the overall reaction pathway of the THPM ring-opening in aqueous-phase conditions is proposed in Fig. 9.

3.2.5. Catalyst recyclability and characterization of spent catalysts

The catalysts structural stability was subsequently evaluated by XRD analysis of spent Ni–zeolite catalysts. To this purpose, after the reaction the catalyst was washed with water, followed by drying under vacuum at 40 °C. As shown in Fig. S12 (Supplementary Material), the XRD patterns of all spent Ni–zeolite catalysts shows a dramatic increase in Ni crystallite size (up to 30–40 nm). This is accompanied with Ni losses by leaching under the hydrothermal condition as reported in Table S5 of Supplementary Material. This is in good agreement with previous studies [47], showing the hydrothermal degradation of catalysts in high-temperature water. Afterwards, the catalytic activity of Ni/ZSM-5 catalyst was examined in a second recycling run, showing 20% loss of its initial catalytic activity due to aggregation of Ni nanoparticles (Table 4, entry 13). This is consistent with TEM measurements of the spent Ni/ZSM-5 catalyst (see Fig. S13 of Supplementary Material). Interestingly, Ni phyllosilicate lamellar structure are still present after recycling run under hydrothermal reaction conditions.

4. Discussion

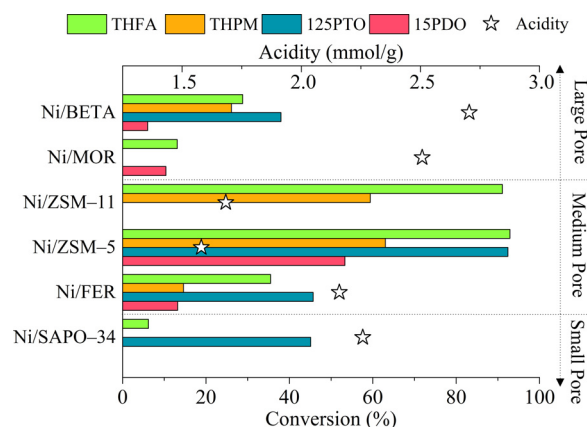
4.1. Formation of Ni phyllosilicate precursors during D-P process

As presented in the result section, various characterization

techniques were employed to elucidate the nature of active sites on the surface of prepared Ni–zeolite catalytic systems. Compared to the bare zeolites, all Ni–zeolites present larger external surface areas, total pore volumes, and mesoporous volumes, but smaller values of BET surface area, microporous surface area and pore volume. This is ascribed to the fact that the deposited Ni species partially block the micropores of the zeolites during the D–P process, while the dissolved silicon species from the zeolite framework react with nickel species to form nickel phyllosilicates on the external surface of the zeolites, leading to the generation of mesoporous surface areas. FTIR, H₂-TPR, XRD, and XPS results suggest that nickel hydroxide species are initially deposited on the zeolite, followed by the generation of poorly crystallized nickel phyllosilicate species and finally 1:1 nickel phyllosilicate, due to the interaction between the nickel hydroxide and the zeolite framework. These species can be decomposed into NiO phase after calcination step, suggesting the presence of a mixture of NiO and 1:1 Ni phyllosilicate species in Ni–zeolite catalysts. For Ni/BETA zeolite, the presence of 2:1 Ni phyllosilicate phase was also confirmed. These findings are in agreement with the previous studies in the literature [22,38].

4.2. Role of zeolite structure on the C–O bond hydrogenolysis of cyclic ethers and polyols

Fig. 10 shows the zeolites maximum pore size compared to the kinetic diameters of cyclic ethers and polyols. It should be mentioned that the maximum pore size of zeolites presented in Fig. 10 are based on Norman radii correction, which is 0.7 Å larger than those calculated with atomic radii (Table S1) [29]. This indicates that all reactants and reaction intermediates can fit inside the zeolites pores with medium and large pores. For SAPO-34 zeolite, the reactants and intermediates molecules are too large to enter the internal porous structure of zeolites and access the acid sites within zeolite pores. This also explains the low reaction rates over Ni/SAPO-34 catalysts owing to its small pore size. Thus, the reaction predominantly takes place on the external surface of

**Fig. 11.** C–O bond Hydrogenolysis of different oxygenates over zeolite-supported Ni nanoparticles. Reaction conditions: 250 °C, 500 psi H₂, 4 h.

SAPO-34.

Comparing different kinds of zeolite structures, zeolites that have medium size pores with 10-membered rings (i.e., ZSM-5 and ZSM-11) exhibited the highest reaction rates in THFA hydrogenolysis reactions. For Ni/FER (intersecting 8-and 10-membered rings), it seems that the presence of 8-membered ring decrease the reaction rate, in spite of the fact that Ni/FER zeolite possesses a higher concentration of acid sites as compared to Ni/ZSM-5 and Ni/ZSM-11 zeolites. The use of MOR and BETA as supports does not improve the catalyst performance, despite the fact that they possess 12-membered ring channels (i.e., large pores) and the highest acid concentrations. Like Ni/FER, the presence of 8-membered channels in the structure of Mordenite seems to decrease the rate of reaction as compared to that of Ni/BETA catalyst. It can be suggested that transition state shape selectivity [28] probably plays a crucial role in the hydrogenolysis of THFA, as well as in the dehydration of the produced pentane polyols, yielding enhanced catalytic activity over Ni/ZSM-5 and Ni/ZSM-11 catalysts. However, it is noteworthy to mention that we did not observe product shape selectivity, according to the nearly similar product distribution obtained over the different tested catalysts [28,29]. The enhanced catalytic performance of Ni/ZSM-5 catalyst prepared by the D-P method can be attributed to a combined effects of different parameters including smaller Ni crystallite size, higher external surface area, as well as higher catalyst acidity due to the generation of phyllosilicate phase, as compared to that of Ni/ZSM-5-IWI catalyst [23].

The product distribution as a function of reaction time also indicates that C–O bond cleavage of THFA into pentane polyols first occurs on active sites on the external surface of the Ni–zeolite catalysts. These produced pentane polyols can be further converted through dehydration pathways. The dehydration pathways can proceed both within the internal zeolite pores and on the external sites, depending on the zeolite structure. For medium and large pores, it is expected that both internal and external active sites contribute to the dehydration pathway, yielding high conversion of 125PTO towards cyclic ether compounds. However, though Ni/BETA catalyst possesses the largest pore size and the highest concentration of acid sites, the lowest catalytic activity is obtained, which might be due to the participation of produced THFA in hydrolysis pathways towards 125PTO. Besides, higher THP yield is obtained over Ni/ZSM-5 catalyst, clearly promoting the subsequent dehydration of both THFA and 125PTO into THP. After all, these findings are in good agreement with the significant difference between reaction rates of THFA hydrogenolysis over Ni supported on different zeolites. It suggests that ZSM-5 framework has a pore confinement effect on the cyclo-dehydration of 15PDO into THP, meaning that the intracrystalline space (i.e., pore intersections) has suitable dimensions for enhancing the catalytic activity for the dehydration pathway [48,49].

The activity trend for THPM hydrogenolysis is well consistent with the one observed for THFA hydrogenolysis, in which Ni supported on ZSM-5 and ZSM-11 showed the highest reaction rate amongst the tested Ni–zeolite catalysts. Additionally, a lower catalytic performance of Ni/ZSM-5 for C₆ diol dehydration to form its corresponding cyclic ether as compared to that of C₅ diol is obtained, leading to higher selectivity towards 16HDO from THPM under similar reaction conditions. Fig. 11 summarizes the catalytic performance during hydrogenolysis reactions over Ni nanoparticles supported on zeolites with various pore sizes and structures. This result demonstrates that the topology of channels and cages within the zeolite pore structure plays a crucial role in the formation rate of cyclic ethers from polyols. Finally, it should be noted that a reasonable correlation between the catalytic performance and catalyst acidity cannot be established.

5. Conclusions

The physicochemical and structural properties of different zeolites, including small pore (SAPO-34), medium pore (Ferrierite, ZSM-5, and

ZSM-11), and large pore zeolites (Mordenite and BETA), were investigated in C–O hydrogenolysis of cyclic ethers (THFA and THPM) and polyols using Ni catalysts. nickel–zeolite catalysts were synthesized via deposition–precipitation (D–P) method and analyzed with a wide range of characterization techniques. The characterization results show the existence of nickel phyllosilicate lamellar structure, along with nickel hydroxide species on the surface of nickel–zeolite catalysts, prepared by D–P method. After calcination, the decomposition of nickel hydroxide into nickel oxide species occurs, while the 1:1 nickel phyllosilicate is transformed into 2:1 nickel phyllosilicate, particularly in the case of Ni/BETA catalyst. Comparing to bare zeolites, larger external surface areas, total pore volumes, and mesoporous volumes are observed for D–P catalysts, owing to the generation of nickel phyllosilicate species. Moreover, the D–P Ni catalysts show smaller particle size due to the improved degree of dispersion of nickel on the zeolite surface, as compared to the Ni/ZSM-5-IWI prepared by impregnation method.

Subsequently, the catalytic activity of prepared catalysts in a C–O bond hydrogenolysis reaction under aqueous–phase condition was investigated. The highest reaction rates are obtained over Ni/ZSM-5 and Ni/ZSM-11 catalysts, with 65–68% selectivity towards THP at 91–93% conversion level. Other zeolites consisting 8- or 12-membered rings exhibit significantly lower catalytic activity, yielding 30–38% 15PDO selectivity at low conversion levels (less than 35%). It can be concluded that C–O bond cleavage of THFA into pentane polyols initially occurs on the external surface of the Ni–zeolite catalysts, followed by further dehydration pathway, which proceeds both within the internal zeolite pores and on the external sites, depending on the zeolite structure. Catalytic tests using the reaction intermediates as reactants suggest that ZSM-5 and ZSM-11 frameworks have pore confinement effect on the cyclo–dehydration of pentane polyols, enhancing the catalytic activity for the dehydration pathway. Regarding the impact of preparation method, D–P Ni/ZSM-5 catalyst shows better catalytic performance in THFA hydrogenolysis as compared to the one prepared by impregnation method. However, it should be noted that D–P Ni/ZSM-5 catalyst still suffers from deactivation due to hydrothermal degradation. For the ring–opening of THPM into 16HDO, the highest reaction rates are again achieved using Ni/ZSM-5 and Ni/ZSM-11 catalysts. The maximum 16HDO selectivity of 51% is obtained over Ni/ZSM-5 catalyst at around 25% THPM conversion. In contrast, the hydrogenolysis pathways to 1-hexanol is more favorable for 16HDO as compared to cyclo–dehydration pathway to produce OXE. This result is further confirmed during the hydrogenolysis of C₆ polyols. It can be concluded that physicochemical properties and porous intracrystalline space of zeolites significantly influence the catalytic performance of Ni–zeolites in biomass conversion. Understanding the effect of zeolite structural topology, therefore, could be a key factor in designing more efficient zeolite catalytic systems for biomass-derived feedstocks.

Acknowledgements

The authors gratefully thank the Singapore Agency for Science, Technology and Research (A*STAR), National University of Singapore, and NEA (ETRP 1501 103) for their generous financial supports. The help of Dr. Liu Dapeng with synthesizing ZSM-11 and SAPO-34 zeolites is also greatly acknowledged. One of us (E.S.) is grateful to A*STAR for the Singapore International Graduate Award (SINGA) scholarship.

Appendix A. Supplementary data

Supplementary material related to this article can be found, in the online version, at doi:<https://doi.org/10.1016/j.apcatb.2018.04.053>.

References

- [1] S.K. Brar, S.J. Sarma, K. Pakshirajan, Platform Chemical Biorefinery: Future Green

- Chemistry, Elsevier, 2016.
- [2] Y. Nakagawa, M. Tamura, K. Tomishige, Catalytic reduction of biomass-derived furanic compounds with hydrogen, *ACS Catal.* 3 (2013) 2655–2668.
 - [3] X. Li, P. Jia, T. Wang, Furfural: a promising platform compound for sustainable production of C4 and C5 chemicals, *ACS Catal.* 6 (2016) 7621–7640.
 - [4] I. Agirrebal-Tellería, J. Reques, M. Giñez, P. Arias, Dehydration of d-xylene to furfural using selective and hydrothermally stable arenensulfonic SBA-15 catalysts, *Appl. Catal., B* 145 (2014) 34–42.
 - [5] Y. Nakagawa, H. Nakazawa, K. Tomishige, Total hydrogenation of furfural over a silica-supported nickel catalyst prepared by the reduction of a nickel nitrate precursor, *ChemCatChem* 4 (2012) 1791–1797.
 - [6] J. Wu, G. Gao, J. Li, P. Sun, X. Long, F. Li, Efficient and versatile CuNi alloy nanocatalysts for the highly selective hydrogenation of furfural, *Appl. Catal., B* 203 (2017) 227–236.
 - [7] S. Koso, N. Ueda, Y. Shinmi, K. Okumura, T. Kizuka, K. Tomishige, Promoting effect of Mo on the hydrogenolysis of tetrahydrofurfuryl alcohol to 1,5-pentanediol over Rh/SiO₂, *J. Catal.* 267 (2009) 89–92.
 - [8] M. Chia, Y.J. Pagán-Torres, D. Hibbitts, Q. Tan, H.N. Pham, A.K. Datye, M. Neurock, R.J. Davis, J.A. Dumesic, Selective hydrogenolysis of polyols and cyclic ethers over bifunctional surface sites on rhodium–rhenium catalysts, *J. Am. Chem. Soc.* 133 (2011) 12675–12689.
 - [9] S. Koso, Y. Nakagawa, K. Tomishige, Mechanism of the hydrogenolysis of ethers over silica-supported rhodium catalyst modified with rhenium oxide, *J. Catal.* 280 (2011) 221–229.
 - [10] S. Koso, H. Watanabe, K. Okumura, Y. Nakagawa, K. Tomishige, Comparative study of Rh-MoO_x and Rh-ReO_x supported on SiO₂ for the hydrogenolysis of ethers and polyols, *Appl. Catal. B* 111–112 (2012) 27–37.
 - [11] T. Buntara, S. Noel, P.H. Phua, I. Melián-Cabrera, J.G. de Vries, H.J. Heeres, Caprolactam from renewable resources: catalytic conversion of 5-hydroxymethylfurfural into caprolactone, *Angew. Chem. Int. Ed.* 50 (2011) 7083–7087.
 - [12] L. Schniepp, H. Geller, Preparation of dihydropyran, 8-hydroxyvaleraldehyde and 1,5-pentanediol from tetrahydrofurfuryl alcohol, *J. Am. Chem. Soc.* 68 (1946) 1646–1648.
 - [13] Z.J. Brentzel, K.J. Barnett, K. Huang, C.T. Maravelias, J.A. Dumesic, G.W. Huber, Chemicals from biomass: combining ring-opening tautomerization and hydrogenation reactions to produce 1, 5-Pentanediol from furfural, *ChemSusChem* 10 (2017) 1351–1355.
 - [14] S.P. Burt, K.J. Barnett, D.J. McClelland, P. Wolf, J.A. Dumesic, G.W. Huber, I. Hermans, Production of 1, 6-hexanediol from tetrahydropyran-2-methanol by dehydration–hydration and hydrogenation, *Green Chem.* 19 (2017) 1390–1398.
 - [15] E. Soghrati, C. Choong, C.K. Poh, S. Kawi, A. Borgna, Single-Pot conversion of tetrahydrofurfuryl alcohol into tetrahydropyran over a Ni/HZSM-5 catalyst under aqueous-phase conditions, *ChemCatChem* 9 (2017) 1402–1408.
 - [16] O.P. Agarwal, Reactions & Reagents Inorganic Chemistry, Goel Publishing House, 1979.
 - [17] J. Falbe, Carbon Monoxide in Organic Synthesis, Springer Science & Business Media, 2013.
 - [18] M.D. Kumbhalkar, J.S. Buchanan, G.W. Huber, J.A. Dumesic, Ring opening of biomass-derived cyclic ethers to dienes over Silica/Alumina, *ACS Catal.* 7 (2017) 5248–5256.
 - [19] M. Romero-Sáez, D. Divakar, A. Aranzábal, J. González-Velasco, J. González-Marcos, Catalytic oxidation of trichloroethylene over Fe-ZSM-5: influence of the preparation method on the iron species and the catalytic behavior, *Appl. Catal., B* 180 (2016) 210–218.
 - [20] S. Kim, G. Park, S.K. Kim, Y.T. Kim, K.-W. Jun, G. Kwak, Gd/HZSM-5 catalyst for conversion of methanol to hydrocarbons: effects of amounts of the Gd loading and catalyst preparation method, *Appl. Catal. B* 220 (2018) 191–201.
 - [21] R. Nares, J. Ramírez, A. Gutiérrez-Alejandre, C. Louis, T. Klimova, Ni/H β -Zeolite catalysts prepared by deposition – precipitation, *J. Phys. Chem. B* 106 (2002) 13287–13293.
 - [22] B.-H. Chen, Z.-S. Chao, H. He, C. Huang, Y.-J. Liu, W.-J. Yi, X.-L. Wei, J.-F. An, Towards a full understanding of the nature of Ni(II) species and hydroxyl groups over highly siliceous HZSM-5 zeolite supported nickel catalysts prepared by a deposition-precipitation method, *Dalton Trans.* 45 (2016) 2720–2739.
 - [23] W. Song, C. Zhao, J.A. Lercher, Importance of size and distribution of Ni nanoparticles for the hydrodeoxygenation of microalgae oil, *Chem. Eur. J.* 19 (2013) 9833–9842.
 - [24] S. Kasakov, H. Shi, D.M. Camaioni, C. Zhao, E. Baráth, A. Jentys, J.A. Lercher, Reductive deconstruction of organosolv lignin catalyzed by zeolite supported nickel nanoparticles, *Green Chem.* 17 (2015) 5079–5090.
 - [25] M.W. Schreiber, D. Rodríguez-Niño, O.Y. Gutiérrez, J.A. Lercher, Hydrodeoxygenation of fatty acid esters catalyzed by Ni on nano-sized MFI type zeolites, *Catal. Sci. Technol.* 6 (2016) 7976–7984.
 - [26] R. Barton, M. Carrier, C. Segura, J. Fierro, N. Escalona, S. Peretti, Ni/HZSM-5 catalyst preparation by deposition-precipitation. Part 1. Effect of nickel loading and preparation conditions on catalyst properties, *Appl. Catal., A* 540 (2017) 7–20.
 - [27] Z. Bian, I.Y. Suryawinata, S. Kawi, Highly carbon resistant multicore-shell catalyst derived from Ni-Mg phyllosilicate nanotubes@silica for dry reforming of methane, *Appl. Catal. B* 195 (2016) 1–8.
 - [28] B. Smit, T.L.M. Maesen, Towards a molecular understanding of shape selectivity, *Nature* 451 (2008) 671–678.
 - [29] J. Jae, G.A. Tompsett, A.J. Foster, K.D. Hammond, S.M. Auerbach, R.F. Lobo, G.W. Huber, Investigation into the shape selectivity of zeolite catalysts for biomass conversion, *J. Catal.* 279 (2011) 257–268.
 - [30] C. Wang, Q. Liu, J. Song, W. Li, P. Li, R. Xu, H. Ma, Z. Tian, High quality diesel-range alkanes production via a single-step hydrotreatment of vegetable oil over Ni/zeolite catalyst, *Catal. Today* 234 (2014) 153–160.
 - [31] A. Lugstein, A. Jentys, H. Vinek, Hydroisomerization and cracking of n-octane and C8 isomers on Ni-containing zeolites, *Appl. Catal., A* 176 (1999) 119–128.
 - [32] D. Liu, Y. Liu, E.Y.L. Goh, C.J.Y. Chu, C.G. Gwie, J. Chang, A. Borgna, Catalytic conversion of ethanol over ZSM-11 based catalysts, *Appl. Catal. A* 523 (2016) 118–129.
 - [33] A. Prakash, S. Unnikrishnan, Synthesis of SAPO-34: high silicon incorporation in the presence of morpholine as template, *J. Chem. Soc. Faraday Trans.* 90 (1994) 2291–2296.
 - [34] R.B. Bird, Transport Phenomena, John Wiley & Sons, New York, 2002.
 - [35] K.G. Joback, R.C. Reid, Estimation of pure-component properties from group-contributions, *Chem. Eng. Commun.* 57 (1987) 233–243.
 - [36] W.M. Haynes, CRC Handbook of Chemistry and Physics, CRC press, 2014.
 - [37] Y.Z. Xiao Kong, Hongyan Zheng, Xianqing Li, Yulei Zhu, Yong-Wang Li, Ni nanoparticles inlaid nickel phyllosilicate as a metal–acid bifunctional catalyst for low-temperature hydrogenolysis reactions, *ACS Catal.* 5 (2015).
 - [38] B.-H. Chen, W. Liu, A. Li, Y.-J. Liu, Z.-S. Chao, A simple and convenient approach for preparing core-shell-like silica@nickel species nanoparticles: highly efficient and stable catalyst for the dehydrogenation of 1, 2-cyclohexanediol to catechol, *Dalton Trans.* 44 (2015) 1023–1038.
 - [39] S. Tomiyama, R. Takahashi, S. Sato, T. Sodesawa, S. Yoshida, Preparation of Ni/SiO₂ catalyst with high thermal stability for CO₂-reforming of CH₄, *Appl. Catal. A* 241 (2003) 349–361.
 - [40] S.M. Auerbach, K.A. Carrado, P.K. Dutta, Handbook of Zeolite Science and Technology, CRC press, 2003.
 - [41] C. Zhao, Y. Yu, A. Jentys, J.A. Lercher, Understanding the impact of aluminum oxide binder on Ni/HZSM-5 for phenol hydrodeoxygenation, *Appl. Catal. B* 132 (2013) 282–292.
 - [42] M. Tamura, K.-i. Shimizu, A. Satsuma, Comprehensive IR study on acid/base properties of metal oxides, *Appl. Catal. A* 433 (2012) 135–145.
 - [43] T. Lehmann, T. Wolff, C. Hamel, P. Veit, B. Garke, A. Seidel-Morgenstern, Physico-chemical characterization of Ni/MCM-41 synthesized by a template ion exchange approach, *Microporous Mesoporous Mater.* 151 (2012) 113–125.
 - [44] K. Huang, Z.J. Brentzel, K.J. Barnett, J.A. Dumesic, G.W. Huber, C.T. Maravelias, Conversion of furfural to 1, 5-Pentanediol: process synthesis and analysis, *ACS Sustainable Chem. Eng.* (2017).
 - [45] S. Sitthisa, T. Sooknoi, Y. Ma, P.B. Balbuena, D.E. Resasco, Kinetics and mechanism of hydrogenation of furfural on Cu/SiO₂ catalysts, *J. Catal.* 277 (2011) 1–13.
 - [46] S. García-Fernández, I. Gandarias, J. Reques, F. Soulímaní, P.L. Arias, B.M. Weckhuysen, The role of tungsten oxide in the selective hydrogenolysis of glycerol to 1, 3-propanediol over Pt/WO_x/Al₂O₃, *Appl. Catal. B* 204 (2017) 260–272.
 - [47] I. Sádaba, M.L. Granados, A. Riisager, E. Taarning, Deactivation of solid catalysts in liquid media: the case of leaching of active sites in biomass conversion reactions, *Green Chem.* 17 (2015) 4133–4145.
 - [48] M.S. Kumar, J. Perez-Ramirez, M. Debbagh, B. Smarsly, U. Bentrup, A. Brückner, Evidence of the vital role of the pore network on various catalytic conversions of N₂O over Fe-silicalite and Fe-SBA-15 with the same iron constitution, *Appl. Catal. B* 62 (2006) 244–254.
 - [49] T. Garetto, E. Rincón, C. Pesteguía, The origin of the enhanced activity of Pt/zeolites for combustion of C₂–C₄ alkanes, *Appl. Catal. B* 73 (2007) 65–72.